ADVANCED FUNCTIONAL MATERIALS
www.afm-journal.de



# Efficient Anisotropic Polariton Lasing Using Molecular Conformation and Orientation in Organic Microcavities

*Florian Le Roux,* Andreas Mischok, Donal D. C. Bradley, and Malte C. Gather**

**Organic exciton-photon polariton lasers are promising candidates for the efficient generation of coherent light at room temperature. While their thresholds are now comparable with those of conventional organic photon lasers, tuning of molecular conformation and orientation as a means to control fundamental properties of their emission and thus further enhance performance remains largely unexplored. Here, a two-fold reduction in the threshold of a microcavity polariton laser based on an active layer of poly(9,9-dioctylfluorene) (PFO) is achieved when 15% $\beta$-phase conformation is introduced. In addtion, taking advantage of the liquid crystalline properties of PFO, a thin photoalignment layer is used to induce nematic alignment of the polymer chains. The resulting transition dipole moment orientation increases the Rabi energy, bringing the system into the ultra-strong coupling regime and facilitating anisotropic polariton lasing with an eight-fold reduction in absorbed threshold, down to 1.14 pJ (0.36 µJ cm$^{-2}$) for the direction parallel to the orientation, with no emission along the orthogonal direction. This represents the first demonstration of anisotropic polariton lasing in conjugated polymer microcavities and a lower threshold than current organic vertical cavity surface-emitting photon and polariton lasers. Dipole orientation offers new opportunities for switchable, more efficient polaritonic devices, and observation of fundamental effects at low polariton numbers.**

## 1. Introduction

A principal ambition of organic electronics has been to realize an electrically driven organic laser diode. However, due to the limited charge carrier mobility and density in organic semiconductors, this has remained largely elusive.[1–5] The accepted strategy to ultimately realize electrically driven organic lasers is to work on reducing the lasing threshold under optical pumping, and thus to eventually bring it into the reach of the population levels achievable under electrical operation. These efforts have traditionally focused on conventional photonic lasers, but the advent of so-called exciton-polariton lasers based on organic materials has been met with great excitement in this context because fundamentally, polariton lasers do not require population inversion and thus might allow lower lasing thresholds.

Exciton-polaritons are hybrid-states of light and matter whose energy signatures can be readily observed in planar microcavities when the interaction between the photonic and the semiconductor excitonic fields become larger than their respective losses. In turn, the separate energy characteristics of light and matter are no longer distinguishable.[6,7] Frenkel excitons found in organic semiconductors possess large binding energies and oscillator strengths[8,9] which, respectively, allow for room-temperature operation and a large Rabi splitting, $\hbar\Omega$, between the lower (LP) and upper (UP) polariton branches; values in excess of 1 eV have been demonstrated in organic microcavities.[10–13] In polariton lasing, polaritons scatter to macroscopically occupy the ground state and then decay through the emission of coherent photons. For organic semiconductors, polariton lasing has been first observed in a high Q-factor planar microcavity containing a single-crystal of anthracene.[14] Following this first demonstration, similar observations were reported in cavities containing layers of small organic molecules,[15] polymers[16] or proteins,[17] where the increased LP lifetime allowed for an efficient thermalization of the LP ground state population, enabling Bose Einstein Condensation (BEC).

Considerable progress has been made in improving the performance of organic polariton lasers; the use of materials exhibiting high photoluminescence quantum yield (PLQY) and fast exciton decay rates has proven particularly beneficial in this context.[18,19] This enabled demonstrations of nonlinear thresholds

F. Le Roux, A. Mischok, M. C. Gather
Humboldt Centre for Nano- and Biophotonics
Department of Chemistry
University of Cologne
Greinstr. 4–6, 50939 Köln, Germany
E-mail: fleroux@uni-koeln.de; malte.gather@uni-koeln.de
D. D. C. Bradley
Physical Science and Engineering Division
King Abdullah University of Science and Technology (KAUST)
Thuwal 23955–6900, Saudi Arabia
M. C. Gather
Organic Semiconductor Centre
SUPA School of Physics and Astronomy
University of St Andrews
St Andrews KY16 9SS, UK

The ORCID identification number(s) for the author(s) of this article can be found under https://doi.org/10.1002/adfm.202209241.



**DOI: 10.1002/adfm.202209241**

in the range 2.2 μJ cm$^{-2}$[18] to 9.7 μJ cm$^{-2}$,[19] values that are now on par with the best organic photon lasers using a vertical cavity surface emitting design.[20,21] In terms of design, adjusting the active layer thickness to target the (0–1) vibronic transition in emission has been shown to be an effective way to further reduce the lasing threshold.[19] However, so far the promise of reaching substantially lower thresholds in polariton lasers than in conventional photonic lasers has not materialized.

Beyond the "holy grail" of electrically pumped organic lasing, lowering the threshold of polariton lasers is also important in other areas. For example, multiple fascinating demonstrations have been made that make use of the quantum nature of polariton condensates, e.g. superfluidity of light,[22] optical logic at room-temperature,[23] and single-photon detection.[24] In many of these devices, the threshold is directly linked to overall device performance and power consumption; thus an effective strategy to reduce thresholds is of great benefit. Other recent work looks into fundamental effects occurring at low polariton numbers.[25,26] In order to explore non-linearities in this regime, low-threshold polariton lasing will be required.

Transition dipole moment orientation is a known method to reduce the threshold for optically pumped exciton gain in poly(9,9-dioctylfluorene) (PFO) waveguides.[27] It has also recently been suggested[28,29] as a way to further reduce the threshold of polariton lasers through efficient population of the LP ground-state. Several material systems have been explored to realize 1D exciton-polaritons, including carbon[30] and tungsten disulfide[31] nanotubes, organic single crystals[32] and liquid crystals,[33] but polariton lasing from such systems remains a challenge. Thin, transparent photoalignment layers of an azobenzene-containing Sulfuric Dye (SD1) have recently been used to induce homogeneous nematic alignment of conjugated polymers in metallic microcavities,[34] leading to significantly enhanced Rabi splitting when the polarization of the incident light is aligned with the polymer transition dipole moment orientation direction. However, these structures have not supported polariton lasing as the alignment has not been realized in a microcavity with sufficiently high Q.

One of the polymers used for alignment induced enhancement of Rabi splitting is PFO. PFO has previously been successfully used to fabricate various electronic/optoelectronic devices (light-emitting diodes (LED)s including polarized light emission structures,[35,36] transistors,[37,38] and optically pumped photon lasers[39]). PFO can also be processed so as to adopt distinct conformations, allowing an exploration of physical structure control over the influence of exciton ensemble sub-populations on polariton formation and properties in metallic microcavities.[40] The disordered glassy-phase possesses an inter-monomer torsion angle centered ≈135°, with a more or less Gaussian distribution of exciton energies.[41] Non-aligned, glassy phase PFO was previously used to demonstrate polariton lasing with an absorbed threshold pump energy density of 19.1 μJ cm$^{-2}$.[42] The linearly-extended $\beta$-phase conformation,[43,44] with a near-to-planar chain segment geometry, presents red-shifted absorption and emission spectra with characteristically-well-resolved vibronic progressions and an enhanced oscillator strength. It forms a distinct exciton sub-population located on the red edge of the glassy Gaussian distribution and the relative weighting of these populations allows polariton properties to be tuned.[40] The $\beta$-phase can be generated in thin films using several different methods, for example: i) globally, via solvent vapour annealing,[44] use of solvent mixtures incorporating a high-boiling point additive,[45] and dipping in a moderate solvent or solvent/non-solvent mixture[44] and ii) locally, via masking[43,46] or dip-pen patterning.[47] Interestingly, PL emission from a sample containing even a small fraction of $\beta$-phase is typically dominated by the spectral contribution of the $\beta$-phase due to rapid energy transfer from the glassy- to the $\beta$-phase chain segments.[44,48]

Here, we use PFO $\beta$-phase generation and nematic liquid crystal alignment to demonstrate an ability to tune the performance of polariton lasers via physical-structure-based, molecular level control of exciton properties. We first fabricate two high-Q microcavities made of distributed Bragg reflector (DBR) mirrors sandwiching spin-coated layers of PFO prepared in the glassy- (sample S1) and $\beta$-phase (sample S2 with 15% $\beta$-phase chain segments) conformations. Both cavities are designed so that the energy of the LP at normal incidence ($\theta = 0°$) is tuned to 2.67 eV, which matches the (0–1) vibronic peak of the $\beta$-phase. We observe that targeting this energy level enables a reduction in the absorbed pump polariton lasing threshold for the glassy-phase cavity to 3.8 μJ cm$^{-2}$ (equivalent to 12.08 pJ per excitation pulse) from the 19.1 μJ cm$^{-2}$ value recorded in earlier reports.[42] Introducing 15% $\beta$-phase then allows for a further twofold reduction in absorbed pump threshold to 1.8 μJ cm$^{-2}$ (5.71 pJ per pulse). In order to study the influence of the polymer chain alignment and corresponding transition dipole moment orientation, we then fabricate a high-Q microcavity containing a layer of PFO which is subjected to thermotropic alignment on a SD1 photoalignment layer, before the generation of 15% $\beta$-phase (sample S4). Orientation of the transition dipole moments in the active layer enables anisotropic coupling in which excitation with a pump polarization parallel to that orientation leads to an over eightfold reduction in absorbed pump threshold from 2.9 μJ cm$^{-2}$ (9.14 pJ per excitation pulse) for an unaligned but otherwise comparable 15% $\beta$-phase cavity (sample S3), to 0.36 μJ cm$^{-2}$ (1.14 pJ per excitation pulse) for the aligned sample S4. The Rabi splitting energies for these structures are substantially enhanced in the direction parallel to the orientation, with the coupling strength $g_1 = \Omega_1/\omega_G$ reaching up to 21.7% and a consequent crossover into the ultra-strong coupling (USC) regime without the need to use metallic mirrors to squeeze the mode volume.[34,40] Using $\beta$-phase generation and nematic liquid crystal alignment allows us to improve the polariton lasing threshold by over 50-fold relative to earlier demonstrations using PFO, and by sixfold relative to the best organic polariton laser reported to date. The absolute absorbed threshold pulse energy of 1.14 pJ is also lower than what has previously been reported for both polariton lasers and conventional photonic lasers based on an organic microcavity structure. As such, our work paves the way to improved polariton devices and makes an important contribution to ongoing efforts on electrically pumped organic lasers.

## 2. Results and Discussion

**Figure 1**a shows the chemical structures of the glassy- and $\beta$-phase chain conformations of PFO and the chemical

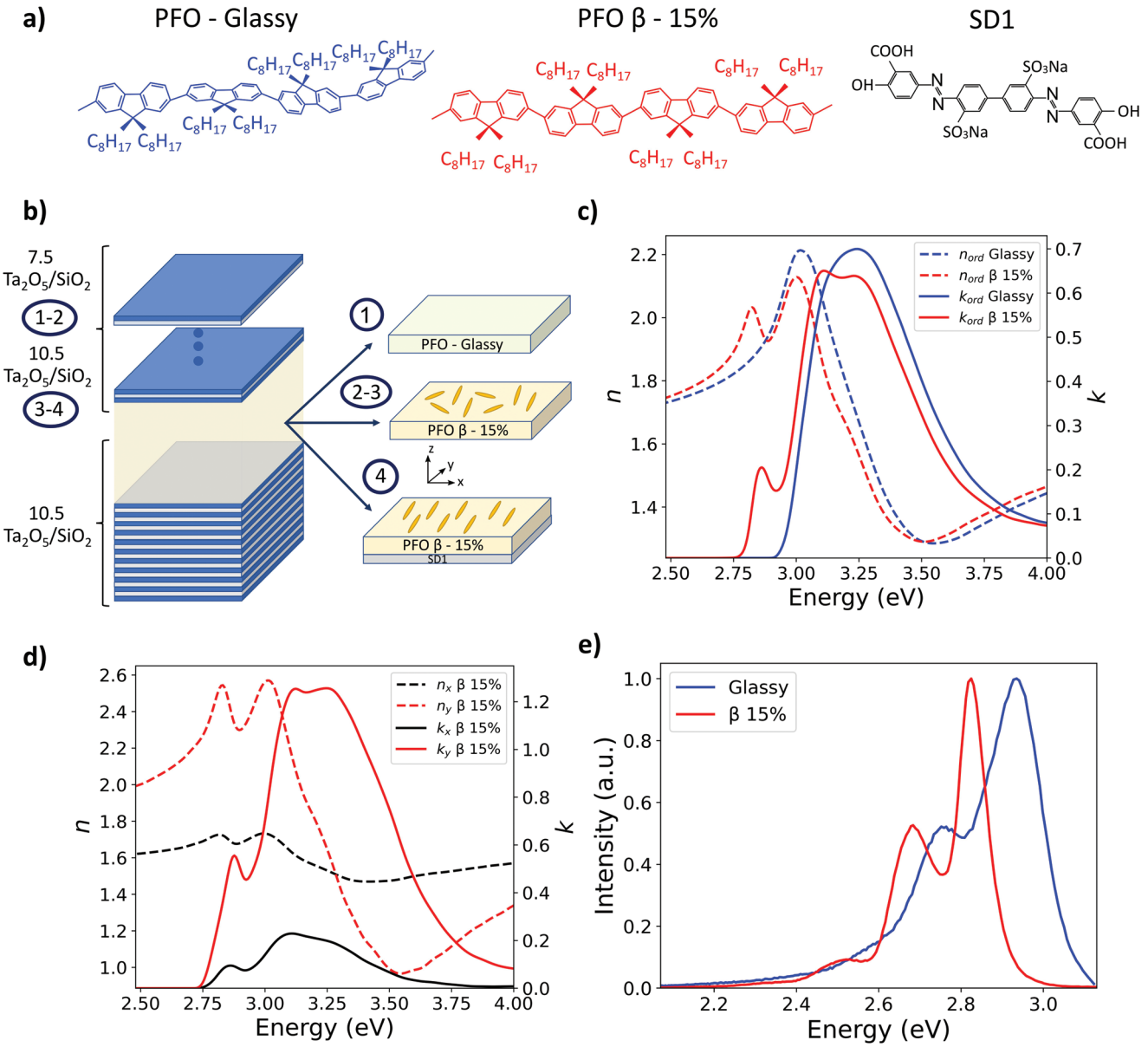


**Figure 1.** a) Chemical structures of the glassy- (blue) and the $\beta$-phase (red) chain conformations of PFO and of SD1 (black). b) Schematic of the different samples (S1, S2, S3, S4) used in this study. c) In-plane optical constants for glassy-phase (blue lines) and 15% $\beta$-phase (red lines) PFO thin films showing the ordinary parts of the extinction coefficient (solid lines), **kord**, and refractive index (dashed lines), **nord**. d) The in-plane, *x*- (black lines) and *y*- (red lines), parts of the extinction coefficient, **kx** and **ky** (solid lines), and refractive index, **nx** and **ny** (dashed lines) for a PFO thin film aligned along the y-direction and subjected to 15% $\beta$-phase generation. e) PL spectra for spin-coated PFO thin films in the glassy phase (blue line) and containing 15% $\beta$-phase (red line).

structure of SD1. Figure 1b shows the schematic structure of the samples used in this study. Sample S1 contains a 155 nm thickness glassy-phase PFO film, S2 a 152 nm thickness 15% $\beta$-phase film, S3 a 166 nm thickness 15% $\beta$-phase film, and S4 a 145 nm thickness 15% $\beta$-phase film aligned on top of a thin layer of SD1 (5 nm). In all samples, the active polymer layers are sandwiched between $Ta_2O_5/SiO_2$ alternating layer DBR mirrors. Samples 1 and 2 have an asymmetric cavity structure with 10.5 $Ta_2O_5/SiO_2$ pairs below and 7.5 above whilst samples 3 and 4 are symmetric cavity structures with 10.5 $Ta_2O_5/SiO_2$ pairs on both sides.

In order to remove any variations in the thickness of the mirror layers between samples as a possible source of error, we deposited the DBRs for pairs of samples at the same time, namely samples S1 and S2 together, and S3 and S4 together. The DBR mirrors for samples S1 and S2 are made of 50.7 nm thickness $Ta_2O_5$/74.4 nm thickness $SiO_2$ alternating layers while for samples S3 and S4 it is 48.8 nm $Ta_2O_5$/71.8 nm $SiO_2$. Similar Q-factors of ≈600 were found for all four samples (calculated from the LP emission linewidth at low excitation energy), i.e., the addition of three further $Ta_2O_5/SiO_2$ pairs in Samples S3 and S4 did not increase the Q-factor at the LP energy

(2.66 – 2.67 eV). We assume that this is due to a combination of two factors: First, beyond 7.5 $Ta_2O_5/SiO_2$ pairs the Q-factor of the cavity saturates as losses other than from incomplete reflection by the mirrors begin to dominate the system, e.g. losses from film roughness. Second, samples S3 and S4 show a slight unintended blue-shift (+0.07 eV) in the stop-band compared to samples S1 and S2 (see Figure S1, Supporting Information). This shift leads to a small increase in reflection loss around the LP energy relative to the centre of the stop-band and therefore the reflectivity of the 10.5 pair mirrors at the LP energy is not significantly enhanced compared to the 7.5 pair mirrors.

The polymer chains of spin-coated PFO films tend to lie within the plane of the film,[42] yielding a uniaxial in-plane/out-of-plane anisotropy in the corresponding optical constants. Figure 1c shows the ordinary components of the measured refractive indices ($\mathbf{n_{ord}}$) and extinction coefficients ($\mathbf{k_{ord}}$), obtained using variable angle spectroscopic ellipsometry (VASE) on films prepared as per samples S1 and S2 on glass substrates. The characteristic, inhomogenously broadened distribution corresponding to the $S_0 - S_1$ optical transition of the glassy-phase of PFO centered at around $X_G = 3.23$ eV is clearly visible. As reported in Ref. [44], the introduction of $\beta$-phase chain segments leads to the appearance of a clearly resolved (0-0) vibronic peak in absorption, which is centered at around $X_\beta = 2.86$ eV. Figure 1d correspondingly shows the in-plane optical constants obtained for a PFO film thermally aligned on top of a SD1 photoalignment layer and then subjected to solvent vapour annealing to induce 15% $\beta$-phase. As expected, the oscillator strength is much stronger in the y-direction (parallel to the orientation of the polymer chains) than in the x-direction, confirming that the transition dipole moment is largely axial. The off-axis component arises from individual dipole moments lying at ≈20–25° to the chain axis for glassy-phase PFO,[49,50] and reduces for the chain-extended $\beta$-phase conformation, leading to a higher anisotropy.[51] Figure 1e shows PL spectra for non-aligned glassy- and 15% $\beta$-phase PFO films. As previously reported,[44,48] the spectra differ substantially: for the glassy-phase film the vibronic peaks appear at 2.93 eV (0-0), 2.75 eV (0–1), and 2.57 eV (0–2) whereas for the $\beta$-phase film the peaks are at 2.82 eV (0-0), 2.67 eV (0–1), and 2.50 eV (0–2).

The deduced refractive indices were used in a transfer matrix calculation to determine the PFO film thicknesses for each sample such that at normal incidence (i.e., $q = 0$) the lower polariton energy, $E_{LP}$, matches the (0–1) emission vibronic peak of the $\beta$-phase at 2.67 eV.

Transverse electric (TE) polarized white light transmissivity spectra were simulated for each sample and for a range of angles of incidence using transfer matrix calculations as shown in **Figure 2**. The simulated spectra are in good agreement with measurements of DBR transmissivity (shown in Figure S1, Supporting Information) as well as angle-resolved reflectivity (shown in Figure S2, Supporting Information) and with polymer thickness measurements using a profilometer. For sample S4, the transmissivity was simulated for an alignment of the polymer chains parallel to the polarization of the incident light (i.e., the azimuthal angle $\varphi$ between the TE-polarization and the alignment direction was 0°). The LP energy was fitted using the Hopfield-Agranovich model[52,53] with one excitonic transition for the glassy phase sample S1 ($X_G$) and two transitions for the $\beta$-phase samples S2, S3, and S4 ($X_G$ and $X_\beta$). The presence of two Rabi splitting energies, $\hbar\Omega_1$ for $X_G$ and $\hbar\Omega_2$ for $X_\beta$, indicates that both conformations contribute as discussed in more detail in Ref. [28]. (The results from the fitting procedure are summarized in **Table 1**.) As discussed in Ref. [15], the experimental observation of the UP in high Q-factor cavities with TE-polarization is very challenging. Rabi energies comparable to or greater than the width of the stop-band are expected,[54] which means the UP falls outside the DBR stop-band. In addition, such high Rabi energies make the direct application of the coupled oscillator model difficult due to further hybridization of the Bragg modes. We therefore confirmed our fitting results by comparing to earlier work that used either the same material (Ref. [42] for S1, Ref. [34] for S2 and S3) or the same alignment technique (Ref. [40] for S4). Reference[40] uses metallic rather than DBR mirrors. While this prevented the realization of polariton lasing, it allows direct observation of the UP as it avoids the limitation of a stop-band with finite spectral width. Based on this UP data, Ref. [40] presents a precise description of the increase in Rabi splitting energy that is expected with transition dipole moment alignment.

Figure 2a shows the optical characterization for S1. The Hopfield-Agranovich fitting yields a Rabi splitting energy of $\hbar\Omega_{1^{S1}} = 0.52$ eV, which is in good agreement with previous reports.[42] The detuning $\Delta_{1G} = -465$ meV between $X_G$ and the energy of the photonic mode at normal incidence $E_{ph}$ ($\theta = 0°$) = $\hbar\omega_{cav,q=0}$ was chosen to be significantly larger than in previous reports in order to target the favorable (0–1) transition. Figure 2b shows the optical characterization for S2, where two detuning energies exist: first, $\Delta_{2G} = -470$ meV similar for the same reason to $\Delta_{1G}$ for S1, and second, $\Delta_{2\beta} = -100$ meV between $X_\beta$ and $E_{ph}(\theta = 0°)$. The ratio of the Rabi energies $\hbar_{1^{S2}} = 0.50$ eV and $\hbar_{2^{S2}} = 0.05$ eV is similar to that found in Ref. [42], where it was shown that the larger oscillator strength of $\beta$- relative to glassy-phase excitons and the interplay of their vibronic structures is important in understanding these coupling strengths. The detuning energies and Rabi splitting values for S3 in Figure 2c are, as expected, similar to those for S2. Notable differences can, however, be found in Figure 2d, where the alignment of PFO chains for S4 increases the Rabi splittings to $\hbar_{1^{S4}} = 0.70$ eV and $\hbar_{2^{S4}} = 0.07$ eV. It was previously observed[33,34] that the increase in Rabi splitting following alignment of the molecular units is due to the increase of the dot product, $\boldsymbol{\mu} \cdot \boldsymbol{E}$, between the molecular transition dipole moment vector, $\boldsymbol{\mu}$, and the incident electric field vector, $\boldsymbol{E}$. Following alignment, the resulting coupling strength $g = \Omega_{1^{S4}}/\omega_G$ reaches 21.7% which brings the system into the USC regime. Previous demonstrations of USC in organic materials have frequently required a cavity formed by metallic mirrors to reduce the mode volume.[10,40]

Next, the angle-resolved emission from the microcavities was measured via Fourier plane imaging. The samples were excited non-resonantly at 355 nm (3.49 eV), using 25 ps pulses from a diode-pumped Nd-YAG laser at a repetition rate of 250 Hz. **Figure 3**a shows the emission from cavity S1 both at low and at high pump pulse energies. At low pulse energies, the emission is spectrally broad and closely follows the fitted LP shown in Figure 2a. Above a certain threshold, however, the emission dramatically reduces in linewidth, blue-shifts, and collapses to

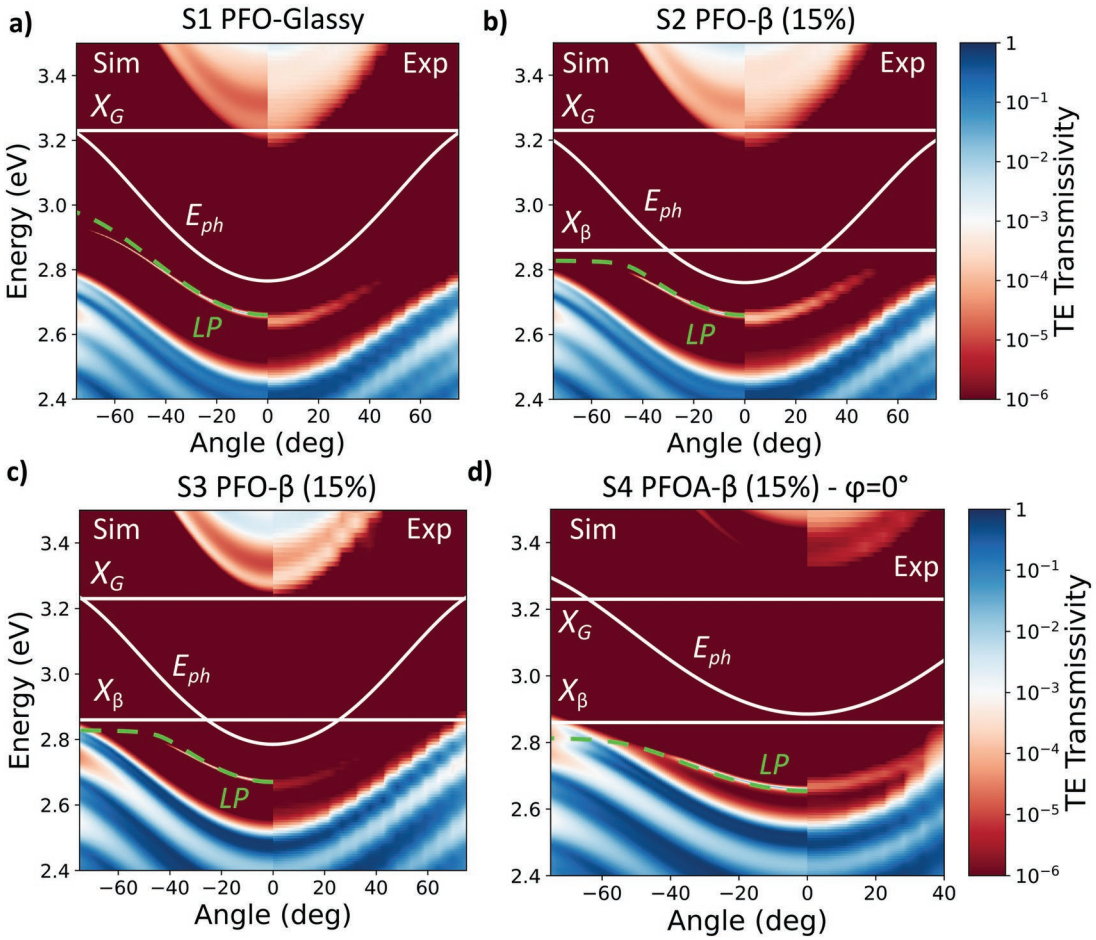


**Figure 2.** Transfer matrix simulations for $\theta$ in the range of [–75°,0°] and experimental measurements for $\theta > 0°$ of angle-resolved, TE-polarized transmissivity spectra for a) sample S1 containing non-aligned glassy-phase PFO, b) and c) samples S2 and S3 containing non-aligned 15% $\beta$-phase PFO, and d) sample S4 containing aligned 15% $\beta$-phase PFO. The horizontal white lines indicate the position of the excitonic transitions $X_G$ and $X_\beta$ as described in the text. The curved white line shows the fitted cavity mode $E_{ph}(\theta) = \hbar\omega_{cav,q}$ and the dashed green line shows the fitted LP mode. For S4, the simulation was performed at $\varphi = 0°$, i.e., PFO polymer chains parallel to the polarization of incident light.

a small angle range around the normal to the plane. Similar observations are made for S2 in Figure 3b and S4 at $\varphi = 0°$ in Figure 3c. Figure 3d shows the emission for S4 at $\varphi = 90°$, where the excitation is perpendicular to the polymer chain alignment. The background-to-emission ratio is higher in Figure 3c,d compared with Figure 3a,b as the overall excitation power was lower due to the decreased threshold for S4 relative to S1 and S2. No emission is recorded from the orthogonal alignment direction due to the strong anisotropy of the system. We also note that in each case, the emission acquires linear polarization parallel to the polarization of the excitation, and, therefore, for S4 also parallel to the chain alignment. When the pump excitation polarization is gradually moved away from the chain alignment direction, it is still possible to observe lasing but with an increasing excitation threshold due to the reducing absorption. The linear polarization acquired by the laser emission from the sample remains,

**Table 1.** Extracted and preset parameter values for microcavities S1, S2, S3, and S4, modeled using a Hopfield-Agranovich Hamiltonian[53,54].

| Sample | $\hbar\omega_{cav}(\theta = 0°)$ [eV][a)] | $\hbar\omega_G$ [eV][b)] | $\hbar\omega_\beta$ [eV][c)] | $n_{eff}$[d)] | $\hbar\Omega_1$ [eV][e)] | $\hbar\Omega_2$ [eV][f)] |
|---|---|---|---|---|---|---|
| S1 (Glassy-phase with 7.5 pair top DBR) | 2.765 | 3.23 | x | 1.88 | 0.52 | X |
| S2 (15% $\beta$-phase with 7.5 pair top DBR) | 2.76 | 3.23 | 2.86 | 1.88 | 0.50 | 0.050 |
| S3 (15% $\beta$-phase with 10.5 pair top DBR) | 2.785 | 3.23 | 2.86 | 1.90 | 0.51 | 0.053 |
| S4 (Aligned 15% $\beta$-phase with 10.5 pair top DBR) | 2.86 | 3.23 | 2.86 | 1.95 | 0.70 | 0.070 |

[a)]Fitted energy of the bare cavity mode at normal incidence; [b)]Preset exciton oscillator transition energy at the peak of the vibronically-unresolved ensemble transition ($S_0$-$S_1$) of glassy-phase PFO films; [c)]Preset exciton oscillator transition energy at the center of the (0-0) vibronic absorption peak of $\beta$-phase PFO films; [d)]Fitted microcavity effective refractive index; [e)]Fitted Rabi splitting energy associated with transition $\hbar\omega_G$; [f)]Fitted Rabi splitting energy associated with transition $\hbar\omega_\beta$.

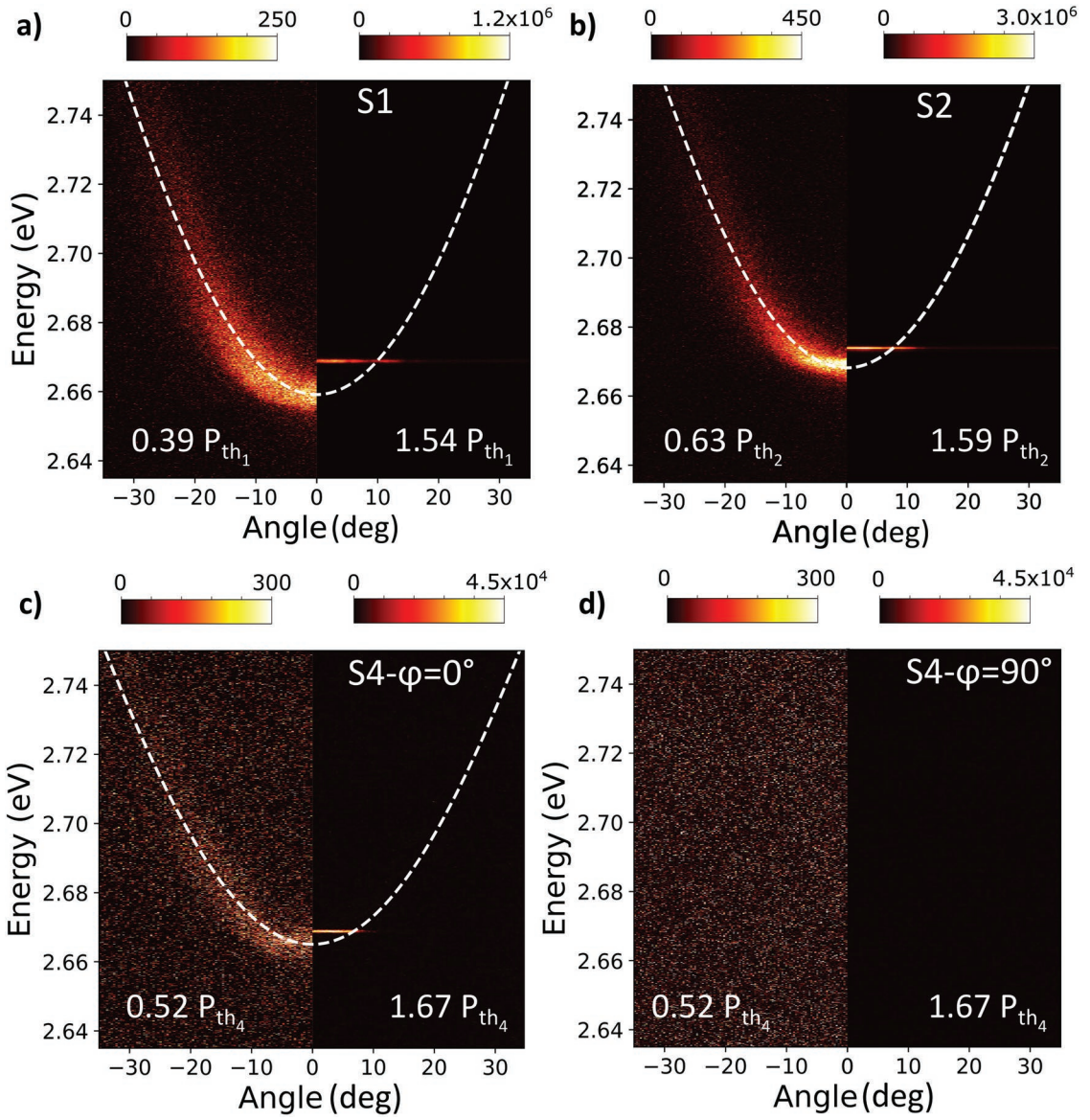


**Figure 3.** Angle-resolved PL spectra intensity maps for microcavities a) S1, b) S2, c) S4 at $\varphi = 0°$ and d) S4 at $\varphi = 90°$ (no emission visible) with emission spectra below (left half) and above (right half) threshold. For each panel, two intensity scales are used.

however, largely parallel to the main component of the transition dipole moment since the "chromophores" that absorb light will emit along the transition dipole moment direction.

**Figure 4**a,c displays for all samples the emission intensity for increasing incident excitation pulse energies, integrated in each case over $\theta \in [-2°; 2°]$ and $E \in [2.635\ \text{eV}; 2.75\ \text{eV}]$. The full PL spectra used for these integrations are shown in Figure S3 (Supporting Information). For each sample, a clear super-linear increase in intensity is observed above a specific threshold excitation energy $P_{\text{th}}$. The saturation in emission intensity observed for S1 and S2 above threshold in Figure 4a was also observed in Ref. [42]. Comparing the pair S1 and S2, we observe that the introduction of 15% $\beta$-phase chain segments in sample S2 leads to a two-fold reduction in threshold pulse energy relative to S1, from $P_{th_1} = 25.16$ pJ down to $P_{th_2} = 12.41$ pJ. We attribute this reduction in threshold to the faster radiative decay of $\beta$-phase excitons[44,55] and the increased overlap of the LP at normal incidence with the (0–1) emission peak of the $\beta$-phase.[19]

Introducing small fractions of $\beta$-phase into glassy PFO films is known to increase the PLQY from ≈55% for glassy PFO films up to almost 70% in an optimal case that can be reached through the use of alkyl additives in the initial solution or with a solvent/non-solvent dipping method.[44,56] However, for the relatively large fraction of $\beta$-phase present in S2, the PLQY is expected to be similar to the glassy PFO of S1,[48] indicating that the reduction in threshold for S2 is most likely not the result of increased PLQY.

In Figure 4c, we observe that the orientation of the transition dipole moments leads to an almost seven-fold reduction in threshold, from $P_{th_3} = 14.50$ pJ for S3 down to $P_{th_4} = 2.23$ pJ for S4. We explain this large reduction through two main

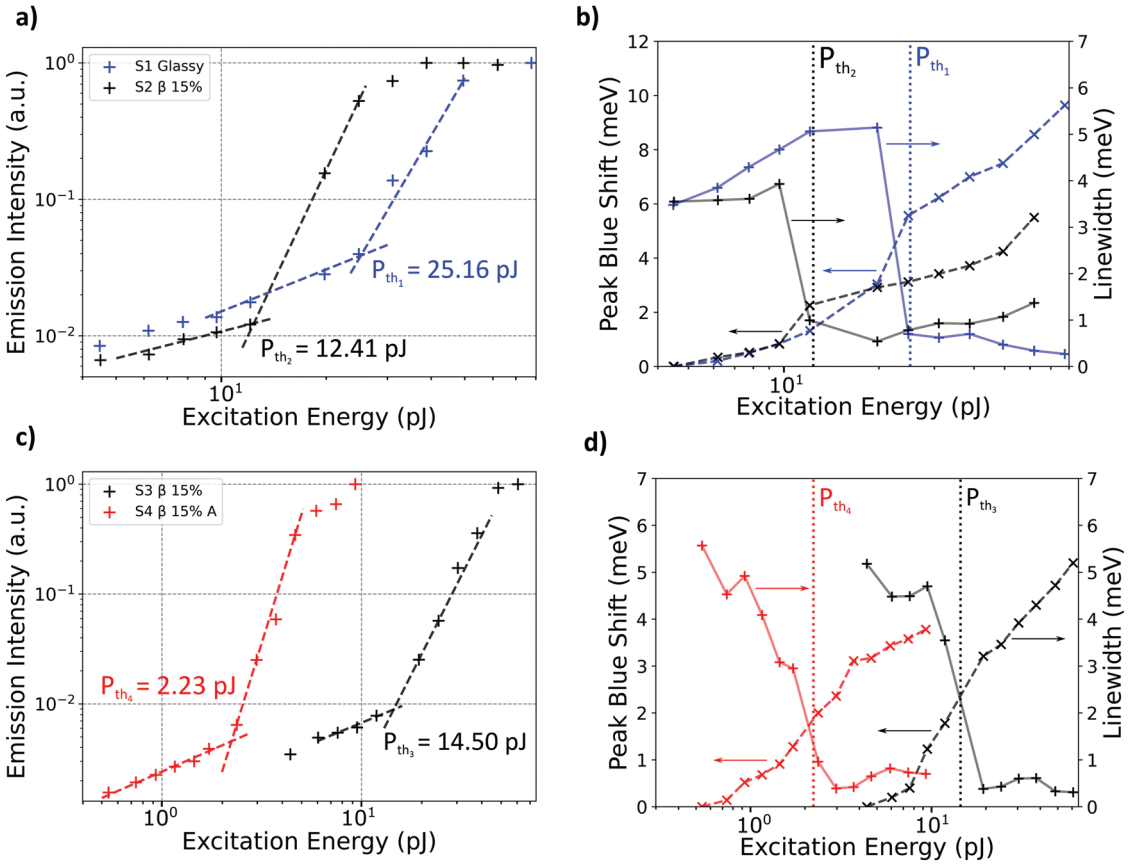


**Figure 4.** a) and c) Integrated emission intensity versus incident excitation pulse energy for a) S1 (blue symbols), S2 (black symbols), c) S3 (black symbols), and S4 (red symbols). The polariton lasing thresholds are determined from the intersects of the fitted dashed lines and are listed next to each data set. b) and d) peak blue-shift (dashed line) and LP linewidth (solid line) for b) S1 (blue) and S2 (black), and d) S3 (black) and S4 (red). Vertical dashed lines indicate the polariton lasing thresholds as determined in a) and c). For S4, the measurements were performed at $\varphi = 0°$.

factors: First, pumping of the exciton reservoir is now twice as effective since the excitation pump polarization is aligned with the main component of the transition dipole moment, second, the LP ground-state is now efficiently populated thanks to an increased rate of resonant excitation transfer from the reservoir to the LP state[29] (this reduction in threshold is simulated in Figure S4, Supporting Information). It is important to note that this reduction is achieved despite additional parasitic absorption introduced by the SD1 layer (Figure S6, Supporting Information). $P_{th_3}$ is slightly larger than $P_{th_2}$ due to the slight blue-shift of the DBR stop-band in S3 and S4 compared to samples S1 and S2 (Figure S1, Supporting Information).

Figure 4b,d displays the linewidth and the spectral shift of the emission peak versus the incident excitation energy per pulse. For each sample we observe a drop in linewidth around the threshold value, corresponding to the increase in coherence acquired as the ground state of the LP is macroscopically populated.[15,16] As the excitation energy increases, we also observe a blue-shift of the emission peak caused by polariton-polariton and polariton-exciton interactions following depletion of the ground state.[15,57]

Combined, the reported observations clearly indicate the presence of polariton lasing for all four samples studied here. Spatial coherence measurements performed on the emission using a retro-reflector configuration Michelson interferometer allows independent corroboration of this conclusion. Above threshold, interference fringes with high visibility are observed (Figure S5, Supporting Information), confirming the presence of spatial coherence and supporting the existence of polariton lasing.

**Table 2** presents a summary of the laser performance parameters for all four samples, comparing the incident and the absorbed pump pulse energy at threshold as well as the corresponding values of threshold pump fluence. To compute the absorbed pulse energy and fluence, the amount of the 355-nm pump light that is absorbed by the PFO film is calculated using transfer matrix calculations[58] (Figure S6, Supporting Information). The excitation pump spot is 20 µm in our experiments. The absorbed threshold fluences are: $F_{th_1} = 3.8\ \mu J\ cm^{-2}$, $F_{th_2} = 1.8\ \mu J\ cm^{-2}$, $F_{th_3} = 2.9\ \mu J\ cm^{-2}$ and $F_{th_4} = 0.36\ \mu J\ cm^{-2}$. We attribute the reduction in $F_{th_1}$, relative to an earlier report for a similar microcavity,[42] to the difference in detuning between the two experiments (≈150 meV), with the experiment presented here bringing the LP energy at normal incidence close to the (0–1) vibronic peak of glassy-phase PFO. The introduction of $\beta$-phase PFO and the preferential orientation of the transition dipoles leads to further dramatic reductions in threshold energy and threshold fluence. To our knowledge, the threshold

**Table 2.** Parameters extracted for polariton lasing thresholds of samples S1, S2, S3, and S4.

| Sample | $E_{LP}$ at $\theta = 0°$, sub-threshold [eV][a)] | Incident threshold pulse energy [pJ] | Intracavity PFO absorption at 355 nm | Absorbed threshold pulse energy [pJ] | Threshold incident fluence [μJ cm$^{-2}$] | Threshold absorbed fluence [μJ cm$^{-2}$] |
|---|---|---|---|---|---|---|
| S1 (Glassy/7.5 pairs top DBR) | 2.66 | 25.16 | 48% | 12.08 | 8.0 | 3.8 |
| S2 ($\beta_{15\%}$/7.5 pairs top DBR) | 2.66 | 12.41 | 46% | 5.71 | 4.0 | 1.8 |
| S3 ($\beta_{15\%}$/10.5 pairs top DBR) | 2.67 | 14.50 | 63% | 9.14 | 4.6 | 2.9 |
| S4 (Aligned, $\beta_{15\%}$/10.5 pairs top DBR) | 2.66 | 2.23 | 51% | 1.14 | 0.71 | 0.36 |

[a)]Energy of LP at normal incidence.

absorbed fluence for polariton lasing in the aligned polymer microcavity, $F_{th_4} = 0.36\ \mu J\ cm^{-2}$, represents the lowest threshold observed to date for organic vertical cavity surface emitting polariton and photon lasers. In addition, the absolute absorbed pulse energy at threshold of 1.14 pJ is possibly the lowest among all organic semiconductor lasers reported so far. Whether pulse fluence or pulse energy is the more important figure of merit depends on the intended application of the laser.

## 3. Conclusion

We have demonstrated how the control of polymer conformation and morphology (specifically chain alignment), together with targeted spectral detuning can be used to improve the performance of PFO organic polariton lasers. First the use of a conformation change from glassy- to 15% $\beta$-phase, together with targeting the corresponding (0–1) vibronic emission peak, halved the absorbed polariton lasing threshold pulse energy and fluence to 5.71 pJ and 1.8 μJ cm$^{-2}$, respectively. The faster radiative decay for $\beta$-phase chain segments is considered to play a key role in this. We then demonstrated that in-plane nematic orientation of the polymer chain transition dipole moments inside the cavity leads to an impressive (more than 8-fold) reduction in absorbed threshold from 9.14 pJ and 2.9 μJ cm$^{-2}$ to 1.14 pJ and 0.36 μJ cm$^{-2}$. Compared to the original, glassy-phase device, the lasing threshold is reduced by over tenfold, and by over 50-fold compared to earlier reports on PFO-based polariton lasers. These improvements in threshold make an important contribution to the ongoing work toward electrically pumped organic lasers and in addition are important to further advance studies into fundamentals of nonlinear polariton interaction.

In the future, a further reduction in lasing threshold can be expected if the position of the stop band of the DBRs is fully optimized in the sample with nematic orientation. In addition, it is anticipated that a further increase in the PLQY of PFO through the use of a lower fraction of $\beta$-phase[44] combined with the use of additional DBR layers should allow a further reduction in threshold. Spatial patterning of the SD1 alignment layer using either a photomask[59] or direct two-photon laser writing[60] represents an additional exciting avenue that may allow further improvement in the performance of polariton lasers through in-plane confinement of polaritons and, additionally, offers the opportunity to study topologic phenomena[61] without a need to pattern the cavity mirrors.

## 4. Experimental Section

*Materials*: PFO was supplied by the Sumitomo Chemical Company, Japan and used as received. The peak molecular weight was $M_{pPFO} = 50 \times 10^3$g mol$^{-1}$. SD1 was supplied by Dai-Nippon Ink and Chemicals, Japan. Anhydrous toluene (99.85%) and anhydrous 2-methoxyethanol (≥99.8%) were purchased from Sigma–Aldrich and used as received. For the microcavity mirrors, $Ta_2O_5$ and $SiO_2$ were sputtered from >99.99% oxide targets (Angstrom Engineering). The substrates used were display-grade glass (Eagle XG, Howard Glass), 24 mm × 24 mm.

*Film Fabrication*: The bare films used for ellipsometry in Figure 1b,c and PL in Figure 1d were spin-coated from 18 mg mL$^{-1}$ PFO solutions in toluene in an inert environment. The solution was prepared in an inert environment (controlled atmosphere nitrogen glovebox with solvent filter) and left to stir overnight at a temperature of 50 °C. It was then filtered using a 0.45 μm PTFE filter. For the sample containing aligned chains of PFO, reported in Figure 1c, a layer of SD1 was first spin-coated (5 s at 500 rpm, followed by 25 s at 2000 rpm) from a 1 mg mL$^{-1}$ solution in 2-methoxyethanol and was then annealed for 10 min at 150 °C to evaporate any traces of solvent. Preparation of the SD1 as an alignment layer was performed in air by exposing the sample to polarized UV light (generated by a UV LED and a broadband polarizer, M365LP1 and WP25M-UB, Thorlabs) at a power of 5 mW for 10 min. A layer of PFO was then spin-coated on top of the SD1 in an inert environment, using 18 mg mL$^{-1}$ PFO in toluene solution, for 1 min at a speed of 2000 rpm, with an initial acceleration of 1000 rpm s$^{-1}$. Next, the sample was placed on a precision hotplate (Präzitherm, Gestigkeit GmbH) in an inert environment and the temperature was raised from 25 to 160 °C at a rate of approximately 30 °C min$^{-1}$. The upper temperature was then held for 10 min, followed by rapid quenching to room temperature by placing the sample on a metallic surface. For three (including the aligned sample) of the four film samples, an approximately 15% $\beta$-phase fraction was induced by exposing the films to a saturated toluene vapour environment for 24 h. The thicknesses of the films and thus of the active layers in the final cavity were measured using a profilometer (Dektak) on simultaneously prepared reference samples and later confirmed by comparing the spectroscopic characterization to transfer matrix calculations.

*Microcavity Fabrication*: The microcavities were fabricated by radiofrequency magnetron sputtering of alternating layers of $SiO_2$ and $Ta_2O_5$ at a base pressure of $10^{-7}$ Torr, using 18 standard cubic centimeters per minute (sccm) Argon flow at 2 mTorr process pressure and 18 sccm Argon together with 4 sccm Oxygen flow at 4 mTorr process pressure for $SiO_2$ and $Ta_2O_5$, respectively. The additional oxygen flow during $Ta_2O_5$ deposition prevents the formation of unwanted sub-oxides. Spin-coating of the active layers was performed on top of the bottom mirror using the same process described in the Film Fabrication paragraph above, except that the concentration of the PFO solution was varied according to the desired film thickness: for S1 and S2, 27 mg mL$^{-1}$ PFO in toluene was used; for S3, 28 mg mL$^{-1}$ was used and for S4, 24 mg mL$^{-1}$. The SD1 alignment layer preparation process for sample S4 followed the description in the Film Fabrication Section above.

*Characterization*: Time-integrated photoluminescence measurements were taken using a fluorescence spectrometer (Picoquant, FluoTime 250) under excitation by a picosecond pulsed laser operating at 375 nm (Picoquant, P-C-375). The permittivity of the different films was determined by variable angle spectroscopic ellipsometry measurements (VASE,

M2000, J.A. Woollam) and subsequent modelling (via CompleteEase software, J.A. Woollam) with a uniaxial anisotropic B-spline for S1, S2, S3 and a biaxial anisotropic B-spline for S4. The transmissivity at normal incidence was determined using the same ellipsometer.

*Polariton Modelling*: The minima of the reflectivity maps shown in Figure 2 were analyzed using a least-squares fitting algorithm for the eigen value problem:

$$H_q \nu_{i,q} = \omega_{i,q} \nu_{i,q} \tag{S1}$$

$$H_q = \begin{pmatrix} \omega_{cav,q} + 2D_q & -i\frac{\Omega_{1,q}}{2} & -i\frac{\Omega_{2,q}}{2} & -2D_q & -i\frac{\Omega_{1,q}}{2} & -i\frac{\Omega_{1,q}}{2} \\ i\frac{\Omega_{1,q}}{2} & \omega_G & 0 & -i\frac{\Omega_{1,q}}{2} & 0 & 0 \\ i\frac{\Omega_{2,q}}{2} & 0 & \omega_\beta & -i\frac{\Omega_{2,q}}{2} & 0 & 0 \\ 2D_q & -i\frac{\Omega_{1,q}}{2} & -i\frac{\Omega_{2,q}}{2} & -\omega_{cav,q} - 2D_q & -i\frac{\Omega_{1,q}}{2} & -i\frac{\Omega_{2,q}}{2} \\ -i\frac{\Omega_{1,q}}{2} & 0 & 0 & i\frac{\Omega_{1,q}}{2} & -\omega_G & 0 \\ -i\frac{\Omega_{2,q}}{2} & 0 & 0 & i\frac{\Omega_{2,q}}{2} & 0 & -\omega_\beta \end{pmatrix} \tag{S2}$$

In the case of a single exciton oscillator, $H_q$ reduces to the usual $4 \times 4$ Hopfield-like USC matrix.[46,47] $q$ is the in-plane wave vector, $\omega_{cav,q}$ the cavity mode energy, $\omega_j$ the frequency for the $j^{th}$-excitons ($j \in \{G,\beta\}$), $\Omega_{j,q}$ the associated Rabi frequency, for a given angle $\theta$, $\Omega_{j,q}(\theta) = \Omega_{0,j}\sqrt{\frac{\omega_j}{\omega_{cav}(\theta)}}$, where $\Omega_{0_j}$ is the Rabi frequency on resonance for the $j^{th}$-transition. In dielectric cavities, $\omega_{cav(TE),\mathbf{q}} = \omega_{cav(TE)}(\theta) = \omega_{cav}(0)\left(1 - \frac{\sin^2(\theta)}{n_{eff}^2}\right)$. $D_\mathbf{q} = \sum_j \frac{\Omega_{j,\mathbf{q}}^2}{4\omega_j}$ is the contribution of the squared magnetic vector potential. The rest of the fitting procedure is identical to that described in Ref. [34].

*Angle-Resolved PL Measurements*: PL spectra were measured using Fourier imaging spectroscopy by imaging the back focal plane of a Nikon Plan Fluor (magnification 40 ×, numerical aperture 0.75) objective, set up on a Nikon Tie2-Eclipse microscope in reflection configuration. The THG output of a diode-pumped Nd-YAG laser (PL2210A, Ekspla), wavelength 355 nm, repetition rate 250 Hz, pulse duration 25 ps, was used for the excitation. Linear polarization of the pump was set by placing a Glan-Taylor polarizer (GT10-A, Thorlabs) before the objective. The diameter of the Gaussian beam at the sample plane was measured to be ≈20 µm. The emitted light was directed toward the entrance of a spectrograph (Shamrock SR-500i-D2-SiL, Andor) equipped with an 1800 lines $mm^{-1}$ grating blazed at 500 nm and the PL spectra were imaged on an EM CCD camera (Newton 971, Andor) providing a spectral resolution of 40 pm. The spatial coherence measurements presented in the Supporting Information were performed using a Michelson interferometer in the retro-reflector configuration and the resulting interferograms were imaged on an sCMOS camera (ORCA-Flash 4.0, Hamamatsu).

## Supporting Information

Supporting Information is available from the Wiley Online Library or from the author.

## Acknowledgements

F.L.R acknowledges funding from the Alexander von Humboldt Foundation through a Humboldt Fellowship. A.M. acknowledges funding from the European Union Horizon 2020 research and innovation programme under the Marie Skłodowska-Curie grant agreement No. 101023743 (PolDev). D.D.C.B. thanks the Sumitomo Chemical Company and DIC Corporation for provision of PFO and SD1, respectively. D.D.C.B. further acknowledges support from King Abdullah University of Science and Technology, Jiangsu Industrial Technology Research Institute (JITRI) and JITRI-Oxford IMPACT Institute (R57149/CN001). This research was financially supported by the Alexander von Humboldt Foundation (Humboldt Professorship to M.C.G.) and by the European Research Council under the European Union Horizon 2020 Framework Programme (FP/2014-2020)/ERC Grant Agreement No. 640012 (ABLASE). The authors are grateful to Prof. Klaus Meerholz and Lukas Böhner for providing access to and support with the VASE ellipsometer.

Open Access funding enabled and organized by Projekt DEAL.

## Conflict of Interest

The authors declare no conflict of interest.

## Data Availability Statement

The data that support the findings of this study are openly available on the St Andrews University repository at https://doi.org/10.17630/b8772acc-16f6-4e19-8105-4988b5e14750, reference number 62.

## Keywords

exciton-polaritons, liquid crystalline conjugated polymers, molecular conformation, molecular orientation, organic semiconductors, polariton lasing

Received: August 17, 2022
Published online:

[1] M. D. McGehee, A. J. Heeger, *Adv. Mater.* **2000**, *12*, 22.
[2] I. D. W. Samuel, G. A. Turnbull, *Chem. Rev.* **2007**, *107*, 1272.
[3] A. J. C. Kuehne, M. C. Gather, *Chem. Rev.* **2016**, *116*, 12823.
[4] C. C. Yan, X. D. Wang, L. S. Liao, *ACS Photonics* **2020**, *7*, 1355.
[5] A. S. D. Sandanayaka, T. Matsushima, F. Bencheikh, S. Terakawa, W. J. PotscavageJr., C. Qin, T. Fujihara, K. Goushi, J. C. Ribierre, C. Adachi, *Appl. Phys. Express* **2019**, *12*, 6.
[6] C. Weisbuch, M. Nishioka, A. Ishikawa, Y. Arakawa, *Phys. Rev. Lett.* **1992**, *69*, 3314.
[7] D. G. Lidzey, D. D. C. Bradley, M. S. Skolnick, T. Virgili, S. Walker, D. M. Whittaker, *Nature* **1998**, *395*, 53.
[8] R. N. Marks, J. J. M. Halls, D. D. C. Bradley, R. H. Friend, A. B. Holmes, *J. Phys.: Condens. Matter* **1994**, *6*, 1379.
[9] S. Alvarado, P. Seidler, D. G. Lidzey, D. D. C. Bradley, *Phys. Rev. Lett.* **1998**, *81*, 1082.
[10] S. Kéna-Cohen, S. A. Maier, D. D. C. Bradley, *Adv. Opt. Mater.* **2013**, *1*, 827.
[11] S. Gambino, M. Mazzeo, A. Genco, O. di Stefano, S. Savasta, S. Patanè, D. Ballarini, F. Mangione, G. Lerario, D. Sanvitto, G. Gigli, *ACS Photonics* **2014**, *1*, 1042.
[12] M. Mazzeo, A. Genco, S. Gambino, D. Ballarini, F. Mangione, O. di Stefano, S. Patanè, S. Savasta, D. Sanvitto, G. Gigli, *Appl. Phys. Lett.* **2014**, *104*, 233303.
[13] M. Suzuki, K. Nishiyama, N. Kani, X. Yu, K. Uzumi, M. Funahashi, F. Shimokawa, S. Nakanishi, N. Tsurumachi, *Appl. Phys. Lett.* **2019**, *114*, 191108.

[14] S. Kéna-Cohen, S. R. Forrest, *Nat. Photonics* **2010**, *4*, 371.
[15] K. S. Daskalakis, S. A. Maier, R. Murray, S. Kéna-Cohen, *Nat. Mater.* **2014**, *13*, 271.
[16] J. D. Plumhof, T. Stöferle, L. Mai, U. Scherf, R. F. Mahrt, *Nat. Mater.* **2014**, *13*, 247.
[17] C. P. Dietrich, A. Steude, L. Tropf, M. Schubert, N. M. Kronenberg, K. Ostermann, S. Höfling, M. C. Gather, *Sci. Adv.* **2016**, *2*, 8.
[18] M. Wei, A. Ruseckas, V. T. N. Mai, A. Shukla, I. Allison, S. C. Lo, E. B. Namdas, G. A. Turnbull, I. D. W. Samuel, *Laser Photonics Rev.* **2021**, *15*, 2100028.
[19] T. Ishii, K. Miyata, M. Mamada, F. Bencheikh, F. Mathevet, K. Onda, S. Kéna-Cohen, C. Adachi, *Adv. Opt. Mater.* **2022**, *10*, 102034.
[20] Y. Hu, F. Bencheikh, S. Chénais, S. Forget, X. Liu, C. Adachi, *Appl. Phys. Lett.* **2020**, *117*, 153301.
[21] A. Mischok, R. Brückner, M. Sudzius, C. Reinhardt, V. G. Lyssenko, H. Fröb, K. Leo, *Appl. Phys. Lett.* **2014**, *105*, 051108.
[22] G. Lerario, D. Ballarini, A. Fieramosca, A. Cannavale, A. Genco, F. Mangione, S. Gambino, L. Dominici, M. de Giorgi, G. Gigli, D. Sanvitto, *Light: Sci. Appl.* **2017**, *6*, 16212.
[23] A. V. Zasedatelev, A. V. Baranikov, D. Urbonas, F. Scafirimuto, U. Scherf, T. Stöferle, R. F. Mahrt, P. G. Lagoudakis, *Nat. Photonics* **2019**, *13*, 378.
[24] A. V. Zasedatelev, A. V. Baranikov, D. Sannikov, D. Urbonas, F. Scafirimuto, V. Y. Shishkov, E. S. Andrianov, Y. E. Lozovik, U. Scherf, T. Stöferle, R. F. Mahrt, P. G. Lagoudakis, *Nature* **2021**, *597*, 493.
[25] G. M. Matutano, A. Wood, M. Johnsson, X. Vidal, B. Q. Baragiola, A. Reinhard, A. Lemaître, J. Bloch, A. Amo, G. Nogues, B. Besga, M. Richard, T. Volz, *Nat. Mater.* **2019**, *18*, 213.
[26] A. Delteil, T. Fink, A. Schade, S. Höfling, C. Schneider, A. İmamoğlu, *Nat. Mater.* **2019**, *18*, 219.
[27] G. Heliotis, R. Xia, K. S. Whitehead, G. A. Turnbull, I. D. W. Samuel, D. D. C. Bradley, *Synth. Met.* **2003**, *139*, 727.
[28] F. Le Roux, *DPhil Thesis*, University of Oxford, **2020**.
[29] T. Ishii, F. Bencheikh, S. Forget, S. Chénais, B. Heinrich, D. Kreher, L. Sosa Vargas, K. Miyata, K. Onda, T. Fujihara, S. Kéna-Cohen, F. Mathevet, C. Adachi, *Adv. Opt. Mater.* **2021**, *9*, 2101048.
[30] W. Gao, X. Li, M. Bamba, J. Kono, *Nat. Photonics* **2018**, *12*, 362.
[31] L. Yadgarov, B. Višić, T. Abir, R. Tenne, A. Yu Polyakov, R. Levi, T. v. Dolgova, V. v. Zubyuk, A. A. Fedyanin, E. A. Goodilin, T. Ellenbogen, R. Tenne, D. Oron, *Phys. Chem. Chem. Phys.* **2018**, *20*, 20812.
[32] S. Kéna-Cohen, M. Davanço, S. R. Forrest, *Phys. Rev. Lett.* **2008**, *101*, 116401.
[33] M. Hertzog, P. Rudquist, J. A. Hutchison, J. George, T. W. Ebbesen, K. Börjesson, *Chem. - Eur. J.* **2017**, *23*, 18166.
[34] F. L. Roux, R. A. Taylor, D. D. C. Bradley, *ACS Photonics* **2020**, *7*, 746.
[35] A. W. Grice, D. D. C. Bradley, M. T. Bernius, M. Inbasekaran, W. W. Wu, E. P. Woo, *Appl. Phys. Lett.* **1998**, *73*, 629.
[36] R. Xia, G. Heliotis, Y. Hou, D. D. C. Bradley, *Org. Electron.* **2003**, *4*, 165.
[37] K. S. Whitehead, M. Grell, D. D. C. Bradley, M. Jandke, P. Strohreigl, *Appl. Phys. Lett.* **2000**, *76*, 2946.
[38] L. L. Chua, J. Zaumseil, J. F. Chang, E. C. W. Ou, P. K. H. Ho, H. Sirringhaus, R. H. Friend, *Nature* **2005**, *434*, 194.
[39] B. K. Yap, R. Xia, M. Campoy-Quiles, P. N. Stavrinou, D. D. C. Bradley, *Nat. Mater.* **2008**, *7*, 376.
[40] F. le Roux, D. D. C. Bradley, *Phys. Rev. B* **2018**, *98*, 195306.
[41] W. Chunwaschirasiri, B. Tanto, D. L. Huber, M. J. Winokur, *Phys. Rev. Lett.* **2005**, *94*, 107402.
[42] M. Wei, S. K. Rajendran, H. Ohadi, L. Tropf, M. C. Gather, G. A. Turnbull, I. D. W. Samuel, *Optica* **2019**, *6*, 1124.
[43] D. D. C. Bradley, M. Grell, X. Long, H. Mellor, A. W. Grice, M. Inbasekaran, E. P. Woo, in *Optical Probes of Conjugated Polymers* (Eds.: Z. V. Vardeny, L. J. Rothberg), SPIE, Bellingham **1997**, p. 254.
[44] A. Perevedentsev, N. Chander, J. S. Kim, D. D. C. Bradley, *J. Polym. Sci., Part B: Polym. Phys.* **2016**, *54*, 1995.
[45] J. Peet, E. Brocker, Y. Xu, G. C. Bazan, *Adv. Mater.* **2008**, *20*, 1882.
[46] G. Ryu, P. N. Stavrinou, D. D. C. Bradley, *Adv. Funct. Mater.* **2009**, *19*, 3237.
[47] A. Perevedentsev, Y. Sonnefraud, C. R. Belton, S. Sharma, A. E. G. Cass, S. A. Maier, J.-S. Kim, P. N. Stavrinou, D. D. C. Bradley, *Nat. Commun.* **2015**, *6*, 5977.
[48] M. Ariu, M. Sims, M. Rahn, J. Hill, M. A. Fox, D. G. Lidzey, M. Oda, J. Cabanillas-Gonzalez, D. Bradley, *Phys. Rev. B* **2003**, *67*, 1.
[49] M. Campoy-Quiles, P. G. Etchegoin, D. D. C. Bradley, *Phys. Rev. B* **2005**, *72*, 045209.
[50] H. Liem, P. Etchegoin, K. S. Whitehead, D. D. C. Bradley, *J. Appl. Phys.* **2002**, *92*, 1154.
[51] M. C. Gather, D. D. C. Bradley, *Adv. Funct. Mater.* **2007**, *17*, 479.
[52] M. Grell, D. D. C. Bradley, X. Long, T. Chamberlain, M. Inbasekaran, E. P. Woo, M. Soliman, *Acta Polym.* **1998**, *49*, 439.
[53] J. J. Hopfield, *Phys. Rev.* **1958**, *112*, 1555.
[54] V. M. Agranovich, *Opt. Spektrosk.* **1957**, *2*, 136.
[55] J. Cao, S. De Liberato, A. Kavokin, *New J. Phys.* **2021**, *23*, 113015.
[56] H. J. Eggimann, F. Le Roux, L. M. Herz, *J. Phys. Chem. Lett.* **2019**, *10*, 1729.
[57] T. Yagafarov, D. Sannikov, A. Zasedatelev, K. Georgiou, A. Baranikov, O. Kyriienko, I. Shelykh, L. Gai, Z. Shen, D. G. Lidzey, P. Lagoudakis, *Commun. Phys.* **2020**, *3*, 18.
[58] G. F. Burkhard, E. T. Hoke, M. D. McGehee, *Adv. Mater.* **2010**, *22*, 3293.
[59] H. Zhang, L. Ma, Q. Zhang, Y. Shi, Y. Fang, R. Xia, W. Hu, D. D. C. Bradley, *Adv. Opt. Mater.* **2020**, *8*, 1901958.
[60] Y. Shi, P. S. Salter, M. Li, R. A. Taylor, S. J. Elston, S. M. Morris, D. D. C. Bradley, *Adv. Funct. Mater.* **2021**, *31*, 2007493.
[61] S. Klembt, T. H. Harder, O. A. Egorov, K. Winkler, R. Ge, M. A. Bandres, M. Emmerling, L. Worschech, T. C. H. Liew, M. Segev, C. Schneider, S. Höfling, *Nature* **2018**, *562*, 552.
[62] F. Le Roux, A. Mischok, D. D. C. Bradley, M. C. Gather, Efficient anisotropic polariton lasing using molecular conformation and orientation in organic microcavities (dataset), St Andrews University Repository **2022**, https://doi.org/10.17630/b8772acc-16f6-4e19-8105-4988b5e14750.